Available online at www.sciencedirect.com
SCIENCE DIRECT®
Wear 259 (2005) 642–650
WEAR
www.elsevier.com/locate/wear

Microstructure and wear mechanisms in C/C composites

Soydan Ozcan, Peter Filip *

Center for Advanced Friction Studies, Southern Illinois University at Carbondale, Carbondale, IL 62901-4343, USA

Received 9 February 2005; received in revised form 11 February 2005; accepted 14 February 2005
Available online 10 May 2005

Abstract

The micromechanisms of the failure and related wear processes in the two-dimensional (2D) randomly chopped and the three-dimensional (3D) non-woven carbon/carbon (C/C) composites with varying fiber type and matrix architecture have been studied by light microscopy, scanning electron microscopy and transmission electron microscopy after the subscale brake dynamometer tests. The instrumented indentation technique (nanoindentation) was used to characterize the localized mechanical properties.

The presented wear model incorporates the formation and propagation of the microcracks within the C/C composites with different matrices and fiber types. Intensive cracking occurred within the highly anisotropic pyrolitic carbon and less frequent cracking was detected in the medium textured carbons on layer/layer levels. The varying mechanical properties (modulus of elasticity) of carbon fiber do not have a significant effect on the micromechanisms of the crack formation and wear. The fracture tip deviates at the fiber/matrix interface in the 2D C/C composite. However, in the 3D C/C composite, the deviation of the advancing crack occurred dominantly within CVI carbon. The crack deflection along the columnar grain boundaries and the crack bridging was observed. Since the frequency of the crack deviation within CVI is very high, an increase in the fracture toughness was detected for 3D samples.

As a result of the different wear mechanisms, different friction layers were formed on the friction surface of 2D and 3D samples. It is possible to optimize the frictional performance of the C/C composites by controlling the microstructure.
© 2005 Elsevier B.V. All rights reserved.

Keywords: Carbon/carbon composites; Wear; Microstructure; Mechanical properties

1. Introduction

The carbon/carbon composite friction materials (C/C) represent one of the most important elements of aerospace, military and higher end commercial vehicle brakes [1–3]. Since the 1960s, they underwent significant development and improvement. The wear and friction mechanisms, however, remain unclear and their better understanding could improve the braking effectiveness and transportation safety.

Wear is defined as a dynamic process of the gradual loss of material from the operating surface of solids as a result of their contact interaction. Mechanism of wear described in literature as dominated by four basic processes of material removal: adhesion, abrasion, surface fatigue and tribochemical reaction [4–8]. There are a number of wear describing equations published in literature. Physical properties (the bulk and the surface) are the most important factors determining wear [9]. The structure/property relationship remains of interest in the area of carbon/carbon composites [10–15]. The industrial and scientific research addressing the manufacturing of the C/C composite friction materials is focused on the low temperature pyrocarbons with the highest deposit rate at the lowest price and an improved frictional and wear property [15,16].

This paper compares the structural and mechanical properties of two commercially available C/C composites. By addressing the effect of the microstructure parameters on the fracture and wear, this study contributes to the understanding of the frictional performance of C/C ceramics.

* Corresponding author. Tel.: +1 618 453 1166; fax: +1 618 453 5260.
E-mail address: filip@siu.edu (P. Filip).

0043-1648/$ – see front matter © 2005 Elsevier B.V. All rights reserved.
doi:10.1016/j.wear.2005.02.112

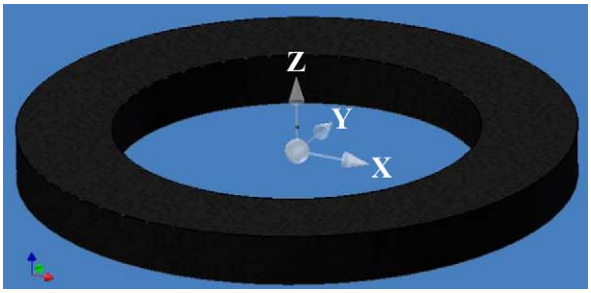

Fig. 1. C/C disc with indication of the applied coordinate system used for description of sample orientation.

2. Experimental procedure

2.1. Materials used

A two-dimensional randomly chopped pitch fibers in charred resin matrix (2D) and a three-dimensional non-woven PAN fiber in CVI matrix (3D) C/C composites were kindly provided by Honeywell International. The "2D randomly chopped" samples have fibers preferentially oriented in the *x–y* plane, while the "3D non-woven" composites contain also carbon fibers oriented perpendicular to the friction surface of the disc (*z*-direction). The schematic view of the brake disc with the chosen coordinate system is shown in Fig. 1.

2.2. Microstructure characterization

A Nikon Microphot-FX polarized light microscope (PLM) was used for the characterization of the microstructure and measurement of the extinction angles of the different pyrocarbons. Three specimens (15 mm × 15 mm × 15 mm) corresponding to different directions (*x*, *y* and *z*) were randomly cut from the two C/C composites. They were mounted in epoxy resin ground and polished using diamond polishing slurries with the grain size from 6 μm down to 0.25 μm. The size of the isochromatic regions was determined and the anisotropy degree of each CVI carbon was evaluated by measuring the extinction angle using PLM [15,18]. The activity of the optical regions is correlated with the orientation of the graphite lamellae. In this study, the distinction of the anisotropic CVI carbon was explained by measuring the extinction angles of each CVI carbon. The optical textures are inferred according to the classification of Duppel et al. [19]. Correspondence between extinction angle (A_e) and the classification of the texture of pyrocarbon is given in Table 1.

Table 1
The textures of the pyrocarbons and the corresponding extinction angles [19]

Textures	Extinction angle (A_e)
Rough laminar	$18° \leq A_e$
Smooth laminar	$12° \leq A_e < 18°$
Dark laminar	$4° \leq A_e < 12°$
Isotropic	$A_e < 4°$

Table 2
Relationship between OA and the different lamellae [14]

Lamillae	Orientation angle (OA)
Rough laminar	$50° \leq A_e$
Smooth laminar	$80° \leq A_e < 50°$
Dark laminar	$180° \leq A_e < 80°$

The full width at half maximum intensity of the azimuthal opening of the (0 0 2) reflection arc is called an orientation angle (OA). The determination of the texture degree was obtained by the measurement of the orientation angle in the (0 0 2) selected area electron diffraction (SAED) pattern using transmission electron microscope (TEM) [3,12,17]. The relationship between OA and the laminar types is reported in Table 2.

The scanning electron micrographs (SEM) of the fracture surfaces of the specimens were obtained using the SEM (Hitachi S570, Tokyo, Japan) to understand the fiber matrix interaction and failure mechanisms. For the TEM studies, thin foils were prepared from 300 μm thick cuts (Linear precision diamond saw, Isomet 4000). Three-millimeter-diameter discs were core-drilled from these cuts (Core Drill, VCR Group, Model V 7110). The discs were mechanically dimpled down to a thickness of about 5 μm (Dimpler, D 500 mechanical dimpler, VCR Group Inc., CA). The ion mill (Ion Tech, FAB 306/TM170, VCR, Group, San Francisco, USA) was employed for the final thinning and polishing stage with a low angle. The TEM studies were carried out using a 125 kV Hitachi H-7100 transmission electron microscope.

2.3. Characterization of mechanical properties

The four-point bending tests were performed according to the ASTM standards (C-1161-026) using the Instron 4206 Mechanical Testing System. The sample size was 45 mm × 9 mm × 5 mm and the load span length of the four-point loading was 40 mm. The tests were performed with a 0.75 mm/min cross-head speed with a 1500 N load cell. For each direction (*x*, *y* and *z*), three samples were tested at room temperature.

The nanoindentation measurements were performed using a fully calibrated Nanoindenter XP system (MTS Nanoinstruments, Knoxville, TN) with a Berkovich-type-pyramid shape diamond indenter. The surface of the samples was prepared by fine polishing in four diamond slurries (in sequence, grain sizes are 6, 3, 1 and 0.5 μm). The displacement resolution for the nanoindenter is less than 0.01 nm, and the load resolution is 50 nN. Before beginning the nanoindentation tests, the system was calibrated using the fused silica. A 10 μm and 300 nm depth indentation was conducted with a Berkovich indenter while the indentation load, *P*, and displacement, *h*, were continuously recorded during one complete cycle of loading and unloading. The Oliver and Pharr method was employed to analyze the nanoindentation data [20].

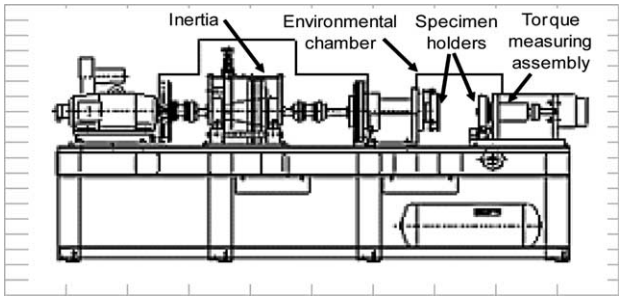

Fig. 2. Scheme of subscale aircraft dynamometer used in research.

2.4. The subscale-dynamometer testing

Friction and wear tests were performed on a subscale aircraft brake dynamometer (Model 2076, Plymouth, MI, USA) using the "ring-on-ring" configuration which simulated the real landing conditions [21]. The schematic picture of the subscale aircraft dynamometer is shown in Fig. 2. The nominal outer and inner diameters of the ring specimens were 92.25 mm (3.75 in.) and 69.85 mm (2.75 in.), respectively.

The friction tests were performed at different fractions (4.5, 12.5, 25, 50, 100 and 200%) of normal landing energy (NLE). Different levels of relative humidity (2, 50 and 90%) were applied. The humidity level was maintained with an advanced test-chamber humidity control system within a 1% of desired value. The subscale aircraft dynamometer was operated in constant torque mode, the normal force varied in response to achieve the desired torque set point. For the period of the braking process, a number of parameters; such as, stop time (7–34 s), braking torque (2.041 kgf m), contact pressure (0.08–0.35 MPa) and speed (202.8 km/h) were controlled. Three taxis and one landing stop sequences were used in testing to simulate operations of a brake. The sequences were repeated 50 times for each energy condition. The initial temperature of each test stop was set up on $T_0 = 49\,^{\circ}\mathrm{C}$ (120 °F) and the applied normal force ramp rate was set up on the value $\mathrm{d}F/\mathrm{d}t = 1780$ N/s (400 lb/s).

The subscale aircraft dynamometer was connected to a computer and particular stops (landing or taxi) were recorded. The coefficient of friction, temperature, torque, decelerating speed and normal force is measured in real time.

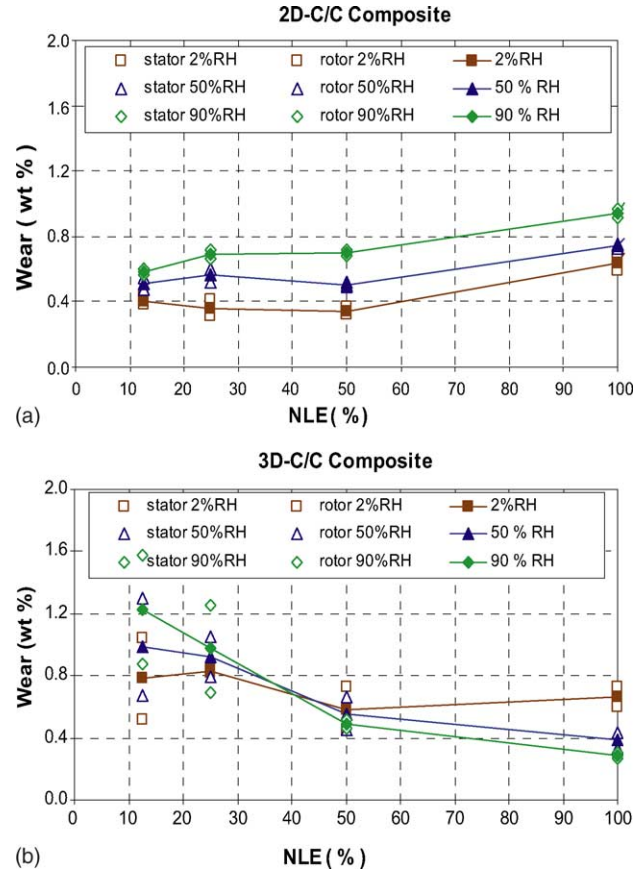

Fig. 3. Wear of two investigated samples 2D (a) and 3D (b), as detected for different simulated energy normal landing energy conditions.

The wear was determined after 200 stops for each condition applied. The wear was expressed as weight loss in the sample using a high precision digital scale. The wear was calculated as:

$$W\,(\%) = \frac{M_\mathrm{i} - M_\mathrm{f}}{M_\mathrm{i}} \tag{1}$$

where W (%) is the wear, M_i the initial mass (always 100 g) and M_f is the final mass (g).

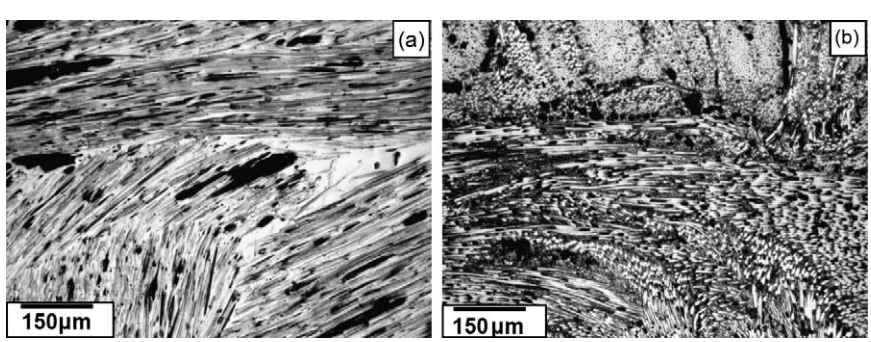

Fig. 4. PLM images taken from friction surface of 2D (a) and 3D (b) samples, respectively.

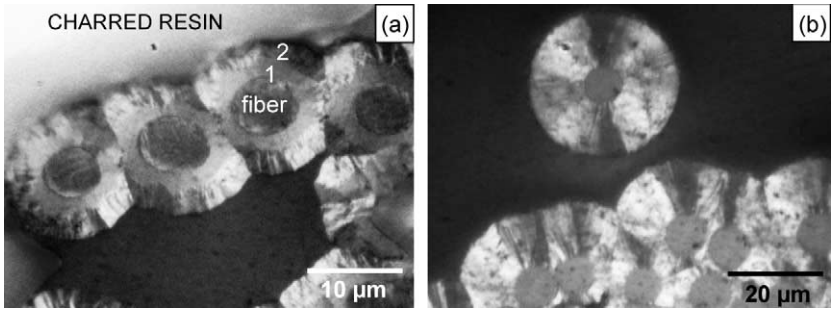

Fig. 5. Detailed microstructure of 2D (a) and 3D (b) material as seen in polarized light microscope.

3. Results and discussion

The wear characteristics of the 2D (HWCCA) and 3D (HWCCD) materials are shown in Fig. 3a and b. A more extensive wearing of the 3D sample is particularly obvious at the lower energies, simulating 12.5 and 25% NLE conditions. An opposite situation was detected at 100% NLE, where 3D materials exhibited higher wear resistance. Almost 100% difference in the wear was detected at different conditions indicate strong influence of C/C microstructure on wear.

The different microstructures are shown in Figs. 4 and 5. The 2D sample consists of randomly chopped, pitch fibers embedded in a charred resin matrix densified by CVI with different degree of anisotropy. The "2D randomly chopped" samples have fibers preferentially oriented in the *x–y* plane (Fig. 4a). The "3D non-woven" composites contain also carbon fibers oriented perpendicular to the friction surface of the disc (*z*-direction) (Fig. 4b). The pitch fibers in 2D composite are surrounded by two lamellae with different degree of optical anisotropy. The first CVI carbon layer in 2D composite exhibited extinction angle, $A_e = 16°$, indicating a smooth laminar microstructure. In contrast, the second CVI layer in 2D composite gave higher extinction ($A_e = 21°$), which is a characteristic of rough laminar pyrolytic carbon. The PAN fibers in the 3D composites are surrounded by one rough laminar layer of carbon with an average extinction angle $A_e = 20°$.

The high magnification TEM bright field images and the selected area diffraction patterns (SAED) corresponding to the fiber, matrix and interface areas are shown in Fig. 6a and b. The pitch fiber in the 2D composite consists of a highly textured microstructure with orientation angle OA = 30° (Fig. 6a), while the PAN fiber in the 3D sample exhibited a slightly less ordered microstructure with OA = 45° (Fig. 6b) [8]. On the contrary, the matrix of the 2D material was less organized (OA = 85°, Fig. 6a) compared to the 3D sample carbon matrix (OA = 60°, Fig. 6b). The fiber/matrix interface is stronger in the 3D material, which forms a semi-crystalline interface (Fig. 6b), while the fiber/matrix interface of 2D sample is typified by the presence of numerous discontinuities (Fig. 6a).

The different mechanical properties of the investigated materials were detected in the nanoindentation (Figs. 7 and 8) and the four-point bending (Fig. 9) experiments. In this study, the 10 μm depth indentations were performed in order to have "a large" indents characterizing of the C/C composites in addition to 300 nm depth indentations respecting to each component of the composites. The SEM images of indentation are given in Figs. 7b and 8c and d. The deeper the indentation, the larger the contact area and both fiber and matrix

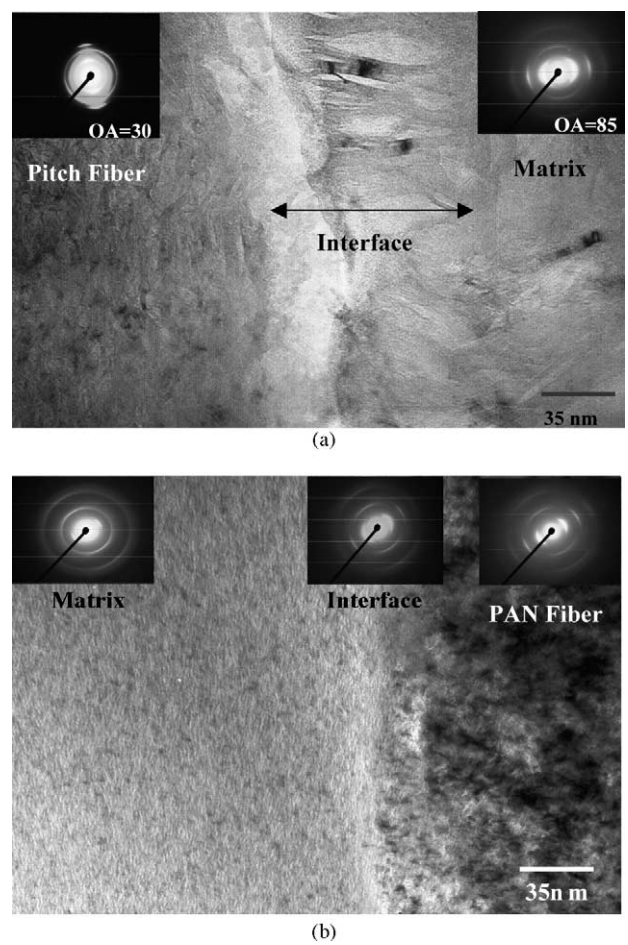

Fig. 6. (a) A TEM bright field image of the 2D material. The inserts represent the SAED patterns from the fiber (left part of the image) and matrix (right part) areas, respectively. (b) A TEM bright field image of the 3D material. The inserts represent the SAED patterns from the fiber (right part of the image), interface (center) and the matrix (left part) areas, respectively. A semi-crystalline interface formed between the C-fiber and the CVI matrix.

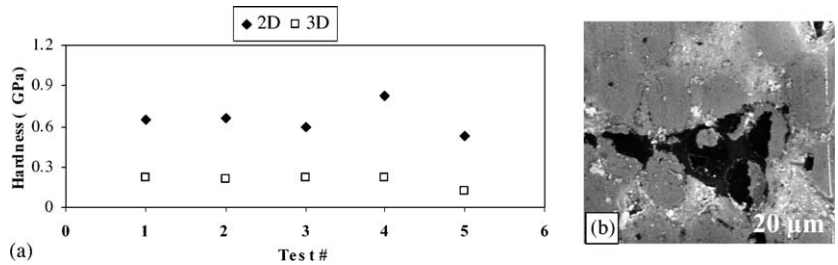

Fig. 7. Nanoindentation results (a) and characteristic indent shape for 10 μm depth test (b) these data represent the properties of entire C/C composites.

properties contribute to the detected hardness value. Fig. 6a summarizes the "10 μm depth nanohardness results" from the five measurements performed with the 2D and 3D samples. As is apparent from Fig. 7b that the fracturing occurred during the indentation, hence, these data does not represent the exact hardness values. Nevertheless, data can be used for a comparison between the 2D and 3D materials, since similar mechanisms were detected into two cases. At low landing energy simulations, the harder 2D composite material wears less when compared to the 3D samples. However, at 100% NLE, the tougher 3D samples exhibited significantly lower wear rate. It is often demonstrated that the wear is inversely proportional to the hardness. Apparently, the increased level of fracture toughness in 3D samples is a relevant factor when

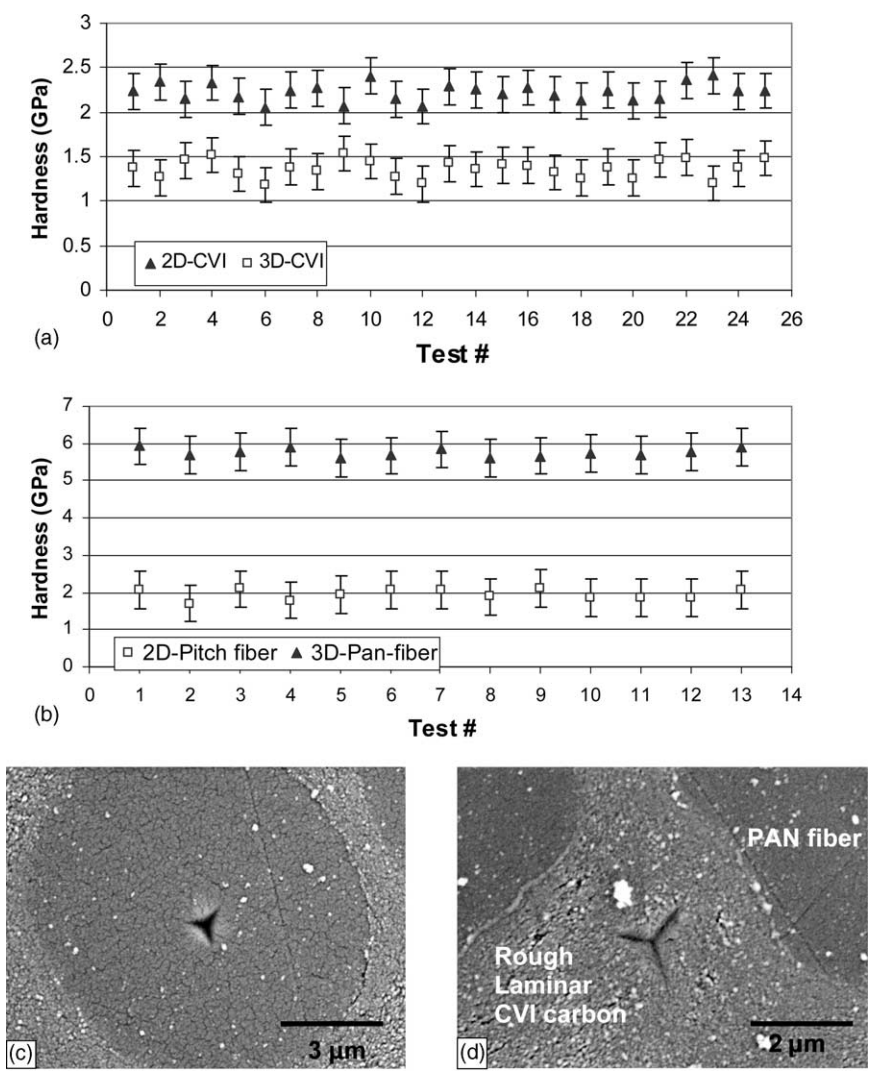

Fig. 8. Hardness data of individual structural components: CVI matrix (a), individual fibers (b) and example images of 300 nm depth tests for 3D C/C composite (c and d), PAN fiber (c) CVI matrix (d).

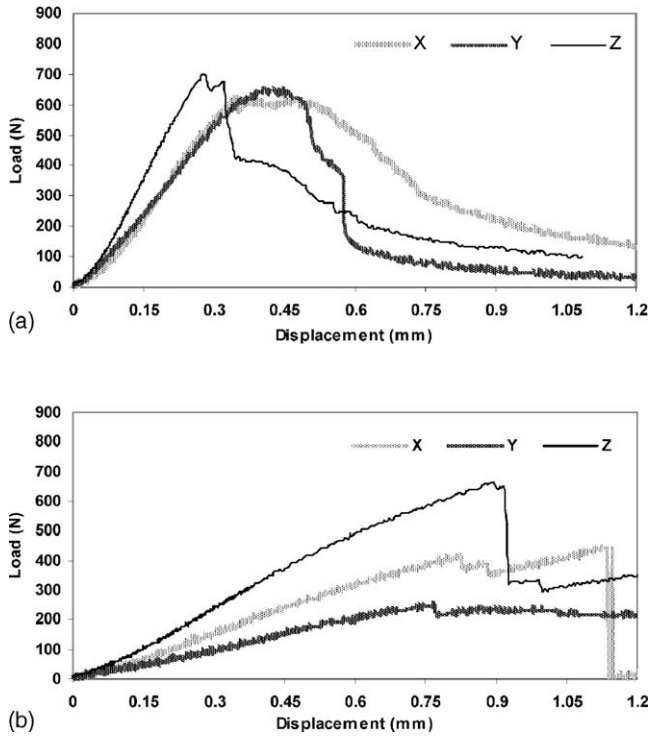

Fig. 9. Load–displacement dependences as detected in the four-point bending tests for the 2D (a) and 3D (b) material.

a more dynamic type of loading with an intense mechanical effect is applied at high speed and energy friction process. The 2D composites containing pitch fibers, charred resin and smooth laminar CVI matrix exhibit more than 100% larger hardness values compared to the 3D sample. The hardness results from 300 nm depth indentation representing individual structural elements of C/C composites are plotted in Fig. 8a and b. Rough laminar CVI carbon in 3D samples exhibited lower hardness than the smooth laminar CVI carbon in 2D samples. Composite hardness of 3D sample is lower than that of 2D sample. The hardness of PAN fibers in 3D samples is three times larger than the hardness of pitch fibers in 2D samples. CVI carbon apparently plays the dominant role in influencing the hardness of C/C composite.

The load–displacement curves obtained from the four-point bending tests are plotted in Fig. 9a (2D material) and Fig. 9b (3D material). It can be seen that the load–displacement curve is almost linear up to the point when the maximum force occurs. For the 2D composite, fracturing was observed at a lower displacement (0.2–0.5 mm), in contrast to the 3D composite (0.8–1.0 mm). The amount of energy dissipated during the fracturing (corresponds to the area beneath load–displacement curve) is higher in the 3D sample as compared to the 2D material. Hence, the 3D material is significantly tougher as compared to the 2D C/C composite. On the other hand, the strength of the 2D samples (maximum

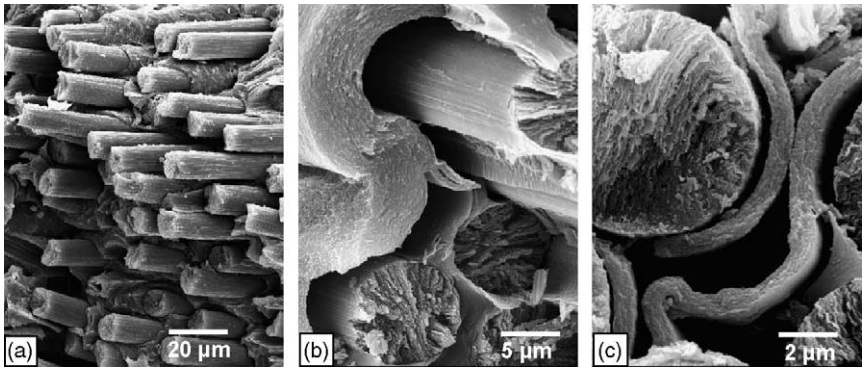

Fig. 10. The fractured surface of 2D sample (a) and detailed in (b and c).

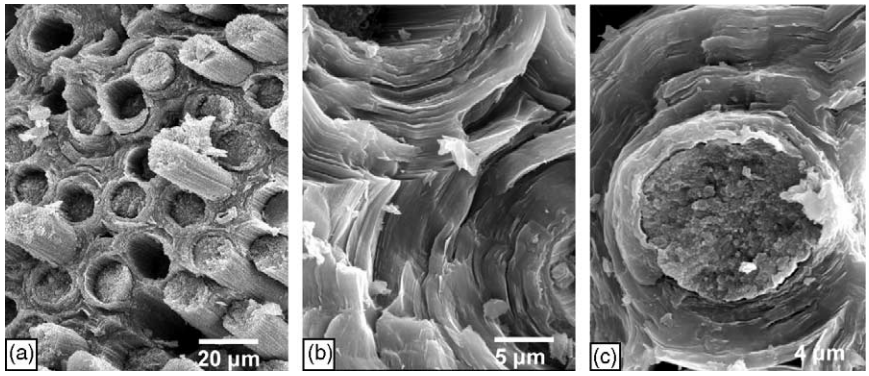

Fig. 11. The fractured surface of 3D sample (a) and detailed in (b and c).

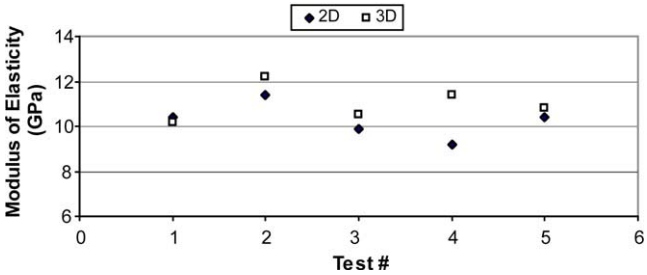

Fig. 12. Elastic module of the 2D and 3D composites.

load before fracture) is higher than the strength of the 3D material, which is in a good correlation with the hardness results.

The SEM analysis revealed the micromechanism of the failure in both composite types (Figs. 10 and 11). Fig. 10a shows that an extensive "pull out" process occurred during the test of 2D samples. Clearly, the weak fiber/matrix interface leads to a fracturing mechanism dominated by the deflection of the microcracks at the fiber/matrix interface. A detailed image shown in Fig. 10b indicates that the CVI carbon separates easily from C-fiber. These findings correspond well with the TEM analysis (Fig. 6a), showing weak interface between C-fiber and charred resin matrix. Fig. 11 shows fracture surface of 3D composite. In contrast to 2D composite a less intensive "pull out" phenomena were detected in 3D composite. Clearly, the 3D composite exhibits a stronger fiber/matrix interaction. A detailed SEM image shown in Fig. 11b reveals that numerous "latent" microcracks within the CVI carbon. Apparently, the fracturing mechanisms in 3D samples are typified by the crack tip deflection between the CVI layers with different textures (Fig. 11c). The crack bridging within the textured CVI levels is frequently detected on the 3D sample fractured surfaces (Fig. 11b). It is possible to expect that the intensity of these effects increases with an increasing load (energy) spent in the wear process. Crack deflection on the fiber/matrix interface was only rarely seen in the 3D samples due to a very good cohesion and formation of the interface between the fiber and matrix (see TEM image in Fig. 6b).

Fig. 12 summarizes the detected moduli of elasticity as obtained from nanoindentation measurements for both composites. As easily seen, the overall module of elasticity of both the 2D and 3D materials were similar (approximately, 11 GPa). The measured values varied from 9.2 to 11.4 for 2D and from 10.2 to 12.2 for 3D materials (Fig. 12). Apparently, the elastic properties (modulus of elasticity) do not have a significant effect on the micro mechanisms of the crack formation and wear in studied C/C composite.

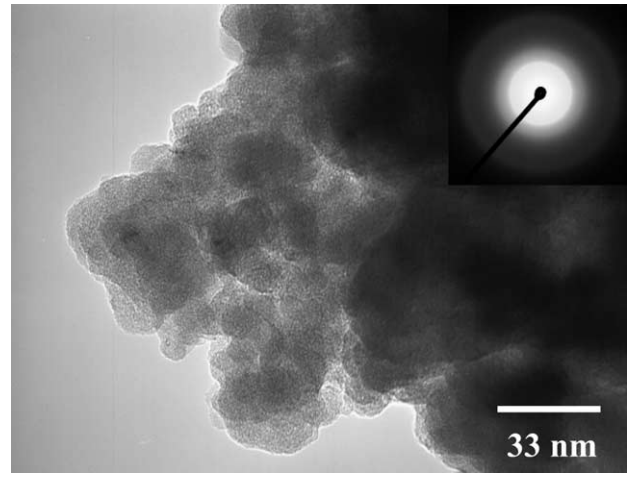

Fig. 13. The bright field TEM image of an amorphous friction layer generated on the surface of the 3D sample. The insert represents the diffraction pattern that was taken from the central part of the bright field image.

A systematic TEM analysis of the friction layer developed on the friction surface of the investigated samples at low energy conditions (12.5 and 25% NLE) revealed that the 3D samples always exhibit the presence of an amorphous friction layer (Fig. 13). In contrast, the 2D materials are characterized by the development of a semi-crystalline friction layer (Fig. 14).

It is obvious from the TEM images that the friction layer consists of the more or less sintered fine wear particles. The micro and nanofracturing mechanisms are apparently the dominant factors leading to the formation of these fine particulates resembling the friction layer.

The more organized structure of the C-fiber and the 2D architecture may have an impact on the crystallinity of the layer developed at low friction energies. Further studies are required in order to provide a detailed explanation of the

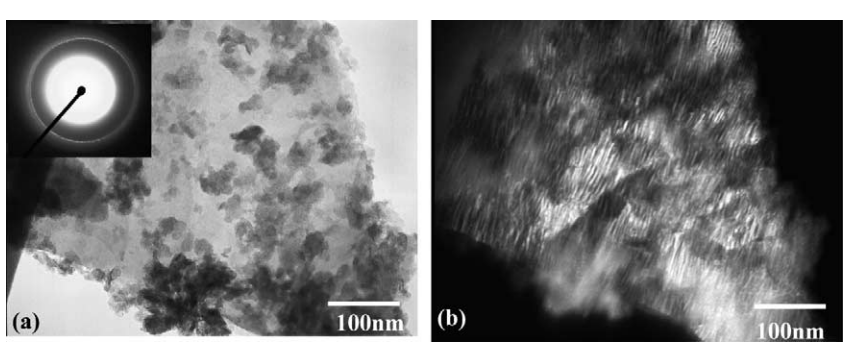

Fig. 14. Bright field TEM image of the semi-crystalline friction layer generated on the surface of the 2D sample (a), diffraction pattern (insert in (a)) from the central part of (a) and the dark field image (b).

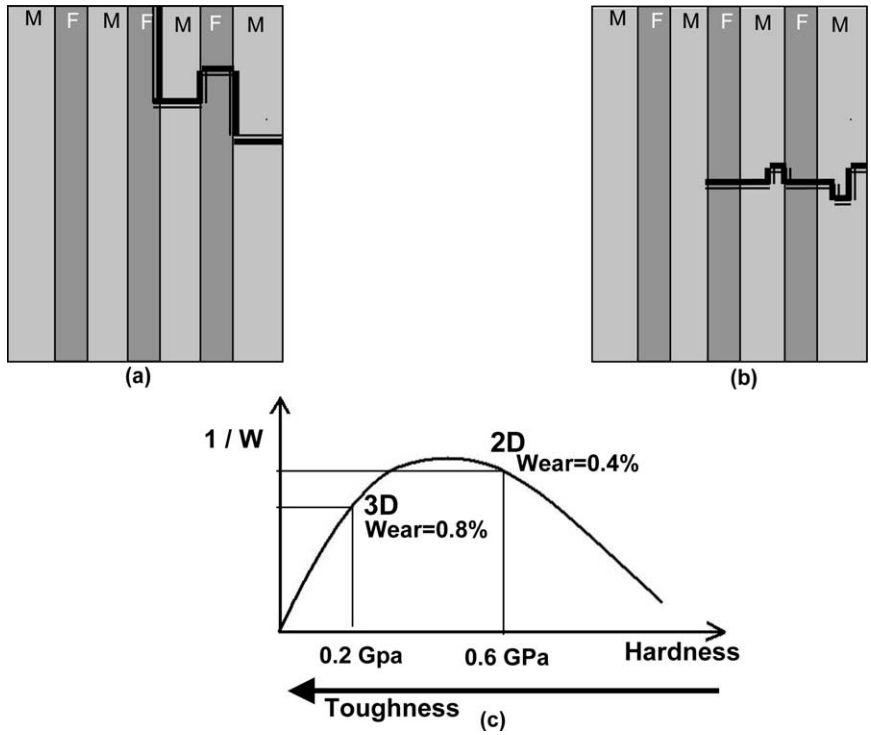

Fig. 15. Schematic of fracture mechanisms of the 2D (a) and 3D (b) composites, and schematic representation of wear dependence on hardness and toughness.

observed interface phenomena. At 100% NLE conditions, both the 3D and 2D samples exhibited a fully amorphous structure of the friction layer (not shown). Apparently, the intensity of the cracking and defect introduction into the C/C materials increases with the increasing energy dissipated during the friction process. Since the surface roughness data indicated only minor differences between the investigated 3D and 2D samples (not shown), it is assumed that the character of the friction layer plays the major role in determining the wear rate. The differences in density and thermal properties of the investigated samples (not shown here) also play a significant role. The temperatures achieved on the surface of the 2D materials are always higher when compared to 3D samples, which may contribute to the particular character of wear, fracturing and friction layer formation.

The fracture advancement and crack deviation is schematically shown in Fig. 15a (2D) and Fig. 15b (3D) for both C/C materials. The wear resistance expressed as inverse value of wear (W), depends on the hardness and fracture toughness of the materials and the schematic picture (Fig. 15c) shows the data for the two investigated samples. It is assumed that the wear performance can be further modified and the optimum wear resistance can be achieved for both samples in cases when the hardness and toughness values of C/C composites optimized.

4. Conclusions

1. The 2D composites containing pitch fibers, charred resin and smooth laminar is harder and exhibits more than 100% larger hardness values compared to 3D sample. The 3D samples are significantly tougher correspond to 2D materials.
2. The microstructure of the C/C composites has a significant effect on the wear of the C/C materials. The harder 2D material wears less than the 3D samples at low energies. However, at 100% NLE, the tougher 3D samples exhibited significantly lower wear rate. It is often demonstrated that the wear is inversely proportional to the hardness. Apparently, the increased level of fracture toughness in 3D samples is a relevant factor when a more dynamic type of loading with an intense mechanical effect is applied at high speed and energy friction process.
3. A friction layer developed on the friction surface seems to be the major factor responsible for the different wear of the samples. This layer consists of crushed and/or sintered fine particulates. Apparently, the cracking/fracturing mechanisms have an effect on the friction layer formation.
4. The elastic properties of C/C composites are similar and do not have a significant impact on the micro mechanisms of the crack formation and wear.
5. It is obvious that by understanding the mechanisms of the wear and friction layer formation, it is possible to optimize the bulk microstructure of the C/C composites.

Acknowledgements

The authors acknowledge the contributions of Milan Krkoska for the performing the friction tests. This research

was sponsored by National Science Foundation (Grant EEC 9523372), State of Illinois and consortium of 12 industrial partners (http://frictioncenter.siu.edu).

References

[1] T. Hutton, B. McEnaney, J.C. Crelling, Structural studies of wear debris from carbon–carbon composite aircraft brakes, Carbon 37 (1999) 907–916.
[2] C.P. Ju, K.J. Lee, H.D. Wu, C.I. Chen, Low-energy wear behavior of polyacrylonitrile, fiber-reinforced, pitch-matrix, carbon–carbon composites, Carbon 32 (5) (1994) 971–977.
[3] N. Murdie, C.P. Ju, J. Don, F.A. Fortunato, Microstructure of worn pitch/resin /CVI C–C composites, Carbon 29 (3) (1991) 335–342.
[4] J.F. Archard, Contact and rubbing of flat surfaces, J. Appl. Phys. 24 (1953) 981–998.
[5] K.C. Ludema, Mechanism-based modeling of friction and wear, Wear 200 (1996) 1–7.
[6] M.M. Khruschov, Principle of abrasive wear, Wear 28 (1974) 69–88.
[7] J. Jiang, F. Sheng, F. Ren, Modeling of two-body abrasive wear under multiple contact conditions, Wear 217 (1998) 35–45.
[8] P. Podra, S. Anderson, Simulating sliding wear with finite element method, Tribology 32 (1999) 71–81.
[9] P. Filip, Friction and wear of polymer matrix composite materials for automotive braking industry, in: International Conference on Braking, 2002, pp. 341–354.
[10] M. Dumont, G. Chollon, M.A. Dourges, R. Pailler, X. Bourrat, R. Naslain, J.L. Bruneel, M. Couzi, Chemical, microstructural and thermal analyses of a naphthalene-derived mesophase pitch, Carbon 40 (2002) 1475–1486.
[11] C. Blanco, E. Casal, M. Granda, R. Menéndez, Influence of fibre–matrix interface on the fracture behavior of carbon–carbon composites, Carbon 23 (15) (2003) 2857–2866.
[12] Z.J. Hu, W.G. Zhang, K.J. Huttinger, B. Reznik, D. Gerthsen, Influence of pressure, temperature and surface area/volume ratio on the texture of pyrolytic carbon deposited from methane, Carbon 41 (2003) 749–758.
[13] V. De Pauw, S. Kalhhofer, D. Gerthsen, Influence of the deposition parameters on the texture of pyrolytic carbon layers deposited on planar substrates, Carbon 42 (2004) 279–286.
[14] X. Bourrat, B. Trouvat, G. Limousin, G. Vignoles, Pyrocarbon anisotropy as measured by electron diffraction and polarized light, J. Mater. Res. 15 (1) (2000) 92–101.
[15] S. Ozcan, P. Filip, Microscopic study of cracking and wear mechanisms in 2D randomly chopped and 3D non-woven C/C composites, in: Proceedings of the International Conference on Carbon, 07/11–07/16, Providence, RI, 2004.
[16] X. Bourrat, Structure of pyrocarbons, in: Fibers and Composites, Taylor & Francis, London & New York, 2003, pp. 159–187.
[17] Z.J. Hu, W.G. Zhang, K.J. Huttinger, B. Reznik, D. Gerthsen, Influence of pressure, temperature and surface area/volume ratio on the texture of pyrolytic carbon deposited from methane, Carbon 41 (2003) 749–758.
[18] E.G. Bortchagovsky, B. Reznik, D. Gerthsen, A. Pfrang, Th. Schimmel, Optical properties of pyrolytic carbon deposits deduced from measurements of the extinction angle by polarized light microscopy, Carbon 41 (2003) 2427–2451.
[19] P. Dupel, X. Bourrat, R. Pailler, Structure of pyrocarbon infiltrated by pulse-CVI, Carbon 33 (9) (1995) 1193–1204.
[20] W.C. Oliver, G.M. Pharr, An improved technique for determining hardness and elastic modulus using load and displacement sensing indentation experiments, J. Mater. Res. 7 (6) (1992) 1564–1583.
[21] T. Policandriotes, T. Walker, P. Filip, Subscale aircraft brake dynamometer testing on C/SiC and C/B4C ceramic friction materials, in: 28th Annual Conference on Ceramics, Metal & Carbon–Carbon Composites, Materials and Structures, Cocoa Beach, FL, January 26–30 (ZAI 1815 N. Forth Myer Drive, Arlington, VA 22209), 2004.